ORIGINAL PAPER

# Investigation of the turbulent wake flow of generic launcher configurations via a zonal RANS/LES method

**V. Statnikov · J.-H. Meiß · M. Meinke · W. Schröder**

**Abstract**  A numerical analysis of the turbulent wake flow of a generic space launcher at supersonic freestream conditions ($Ma_\infty = 6.0$ and $Re_D = 1.7 \times 10^6$) is performed using a zonal RANS/LES method. To investigate the influence of various components of a rocket model on the base flow, three supported wind tunnel configurations with the same main body geometry and different aft-body extensions consisting of a blunt base, a nozzle dummy, and a full flowing underexpanded TIC nozzle ($Ma_e = 2.52$, $p_e/p_\infty = 100$) are considered. Flow topologies for three cases are described in detail including an estimate of the impact of the wind tunnel model support on the flow field. To validate the applied numerical method, the computed flow fields are compared to experimental data from high-speed schlieren measurements provided by DLR Cologne. The influence of the used aft-body extensions on the steady-state and dynamic base flow characteristics is evaluated by a detailed analysis and comparison of the pressure distribution and its spectra along the base and nozzle walls for three investigated configurations. The numerical findings are compared to experimental wall pressure oscillation measurements provided by DLR Cologne. The major results are the non-negligible influence of the model support on the wake even on the strut averted side, the base drag reduction effect of the aft-expanding jet plume consisting of an increase of the base pressure level from $p/p_\infty \approx 0.2 - 0.25$ (blunt base and nozzle dummy configurations) up to $p/p_\infty \approx 0.7$ leading to a decrease of the base pressure drag coefficient from $C_{Dp\ base} = 0.032$ to $0.012$ correspondingly, and the identified dominant low-frequency modes of the base pressure oscillations at $Sr_D \approx 0.05$, $Sr_D \approx 0.1$, and $Sr_D \approx 0.2$ also detected in the experiments.

**Keywords**  Zonal RANS/LES · Hypersonic wake · Space launcher aerodynamics

V. Statnikov (✉) · J.-H. Meiß · M. Meinke · W. Schröder
Institute of Aerodynamics, RWTH Aachen University,
Wüllnerstraße 5a, 52062 Aachen, Germany
e-mail: V.Statnikov@aia.rwth-aachen.de

## 1 Introduction

An accurate prediction of the base flow physics of rockets still poses a great challenge in developing future rocket-like launch vehicles. Although in most cases the base geometry is quite simple, the flow field is determined by different intricate phenomena, such as flow separation at the base shoulder, reattachment of the shear layer at the outer nozzle wall, interaction with the jet plume, to name a few. It is generally known that the base drag of axial cylindrical bodies, which is caused by the low pressure associated with the recirculation area at the base, constitutes a major part of the overall drag. Rollstin [1], for instance, determines the base drag of projectiles caused by the separation of the outer flow to be up to 35 % of the overall drag, which can be even higher for launch vehicles due to their larger base area. Moreover, the involved base flow phenomena possess a pronounced unsteady behavior. At supersonic speeds and higher altitudes the nozzle usually operates at underexpanded mode with a strongly aft-expanding jet plume. The displacement effect on the base flow generated by a wide jet plume leads to an increase of the base pressure level and consequently, to a reduction of the base drag. On the other hand, the periodic and stochastic base pressure oscillations become stronger and

might excite vibrations of critical amplitude. Besides the mentioned aero-elastic aspect, convection of the hot gases from the jet upstream to the base area can lead to confined hot spots and thermal loads of the structure. Therefore, it is of fundamental importance to provide accurate analyses of the not yet fully understood static and dynamic behavior of the base flow for the design and optimization of reliable future space launcher systems.

Numerous investigations of the separated base flow of space launchers have been performed in the past experimentally and numerically. The majority of the work is based on the experiments by Dutton et al. [2], who investigated an axisymmetric configuration at $Ma_\infty = 2.46$, by Bannink et al. [3], and by Scarano et al. [4] who examined an axisymmetric rocket configuration at $Ma_\infty = 2$ and $Ma_\infty = 3$ with an underexpanded Mach 4 nozzle flow in the context of the FESTIP (Future European Space Transportation Investigations Programme) research program. Turbulence models used in the numerical studies range from various Reynolds-averaged Navier–Stokes (RANS) models [5, 6] via detached-eddy simulations (DES) [7, 8] and large-eddy simulations (LES) [9] to direct numerical simulations (DNS) [10, 11, 12]. The base flow and the base pressure, however, have not always been predicted with sufficient accuracy. Especially, RANS models were found to be not capable of predicting accurate unsteady data and also fail to provide accurate results concerning the low pressure recirculation area behind the base, while the predictions of the attached flow around the main body are quite satisfactory. DNS is at the present time restricted to small Reynolds numbers and a small integration domain. Therefore, a zonal RANS/LES approach is applied in this work to investigate the base flow of a generic launcher, i.e., RANS simulations are used to predict the attached flow field along the main body and vertical strut support, while LES is applied to the unsteady wake flow using time-averaged velocity profiles combined with time-resolved synthetically generated turbulent fluctuations reconstructed from the upstream RANS results as inflow conditions.

## 2 Geometry and flow condition

The generic rocket configurations investigated in this work correspond to the wind tunnel models experimentally studied at DLR Cologne and DLR Braunschweig within the research program Transregio 40. They incorporate three setups of a generic space launcher differing only in the aftbody extensions, i.e., a blunt base, a nozzle dummy, and a full-flowing nozzle. The basic rocket consists of a rounded conical top with an apex angle of 36° and a cylindrical main body part with a diameter of 108 mm. Like in the accompanying experimental investigations, a vertical double-wedge profiled strut is orthogonally attached to the upper side of the main body due to the necessity to mount the models in the wind tunnel and to enclose cables for the electronics and gas supplies for the nozzle flow. An overview of the configurations and the geometry parameters is presented in Fig. 1.

The flow conditions of the numerical simulations ($Ma_\infty = 6$ and $Re_D = 1.7 \times 10^6$) follow the experimental set up and are summarized in Table 1. The Mach and Reynolds numbers are based upon a typical supersonic stage of the ascent trajectory of the European Ariane V launcher. The configuration with a nozzle jet possesses a full-flowing truncated ideal contour (TIC) nozzle with an averaged Mach number of $Ma_e = 2.52$ and a pressure ratio of $p_e/p_\infty = 100$ at the exit leading to a strong aft-expansion of the jet.

## 3 Computational approach

### 3.1 Flow solver

An in-house structured multi-block flow solver is used for the simulations. The Navier–Stokes equations are solved for three-dimensional unsteady compressible flow based on a LES using the monotone integrated LES (MILES)
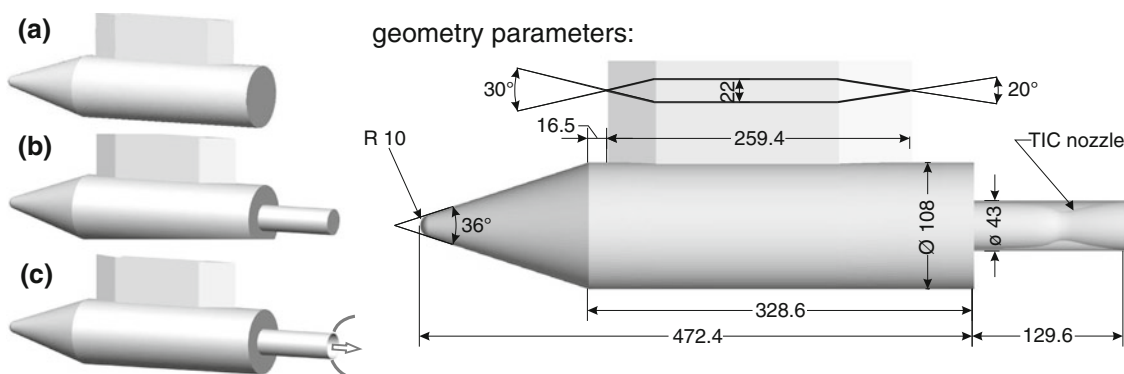


Fig. 1 *Left* Investigated configurations: **a** blunt base; **b** nozzle dummy; **c** full-flowing nozzle. *Right* Geometry parameters of the wind tunnel model with jet

**Table 1** Freestream and nozzle flow conditions

|  | Ma | $Re$ (1/m) | $u$ (m/s) | $p_0$ (Pa) | $p$ (Pa) | $T_0$ (K) | $T$ (K) |
|---|---|---|---|---|---|---|---|
| Freestream ($\infty$) | 6.0 | $1.6 \times 10^6$ | 910 | $18 \times 10^5$ | $1.14 \times 10^3$ | 470 | 57 |
| Nozzle flow (exit) | 2.5 | $24 \times 10^6$ | 900 | $20 \times 10^5$ | $109 \times 10^3$ | 470 | 204 |

approach [13] formulated on a vertex-centered block-structured mesh. A modified advection-upstream-splitting method (AUSM) is used for the Euler terms [14] which are discretized to second-order accuracy by an upwind-biased approximation. For the non-Euler terms a centered approximation of second-order accuracy is used. The temporal integration from time level $n$ to $n + 1$ is done by a second-order accurate explicit 5-stage Runge–Kutta method, the coefficients of which are optimized for maximum stability. For a detailed description of the LES solver the reader is referred to Meinke et al. [15]. The RANS simulations use the one-equation turbulence model of Fares and Schröder [16] to close the averaged equations.

### 3.2 Reformulated synthetic turbulence generation (RSTG) method

According to the applied zonal RANS/LES approach, the attached flow field along the main body and strut support of the rocket models is determined by a RANS simulation, while for the highly unsteady wake flow region a time-resolved LES is used, Fig. 2. The challenging transition from the RANS to the LES zone is performed by a Reformulated Synthetic Turbulence Generation (RSTG) Method developed by Roidl et al. [17, 18] that allows a reconstruction of the time-resolved turbulent fluctuations from the time-averaged upstream RANS solution.

The RSTG method is based on the synthetic eddy method (SEM) of Jarrin et al. [19] and Pamiès et al. [20] and describes turbulence as a superposition of coherent structures. These structures are generated over the LES inlet plane by superimposing the influence of virtual eddy cores which are defined in a virtual volume $V_{virt}$ around the

inlet plane that has the streamwise, wall-normal, and spanwise dimensions of the turbulent length scale $l_x$, the boundary-layer thickness at the inlet $\delta_0$, and the width of the computational domain $L_z$. The turbulent length scales that describe the spatial properties of the synthetic structure are scaled with the Reynolds number and the associated convection velocity depends on the distance from the wall. A detailed description of the method including the shape functions and length scale distributions is given in [17].

### 3.3 Computational grids

Since the main body geometry is identical for all considered cases, a modular setup is used for the computational grids that consists of using the same RANS mesh for the main body and three different LES meshes for the applied aft-body extensions. To illustrate the applied grid topologies, the meshes for the RANS and LES zones used for the configuration with jet are shown in Figs. 3 and 4. To reduce computational costs, the grids span a region of 180° with a mirror boundary condition in the symmetry plane. The RANS grid for the main body ranges from $-8D$ to $0D$ in the streamwise and up to $4D$ in the radial direction with $D$ being the diameter of the cylindrical main body part and the origin of ordinates lying in the center of the rocket base. The RANS/LES transition plane is at $x = -0.25D$ upstream of the base shoulder with the boundary layer thickness being $\delta = 0.12D$ which yields a satisfactory transition length of approximately $2\delta$ as expected by the RSTG method. The LES grid spans between $x = -0.25D$ and $x = 3.2D$ in the streamwise and up to $3.6D$ in the radial direction in the above mentioned coordinate system.
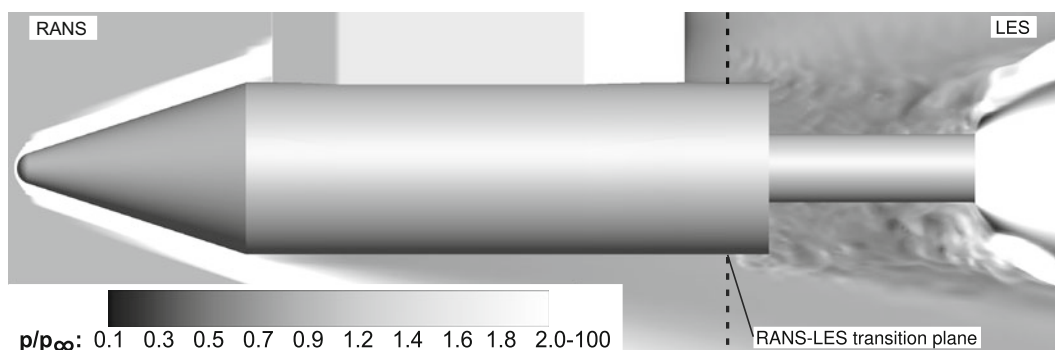


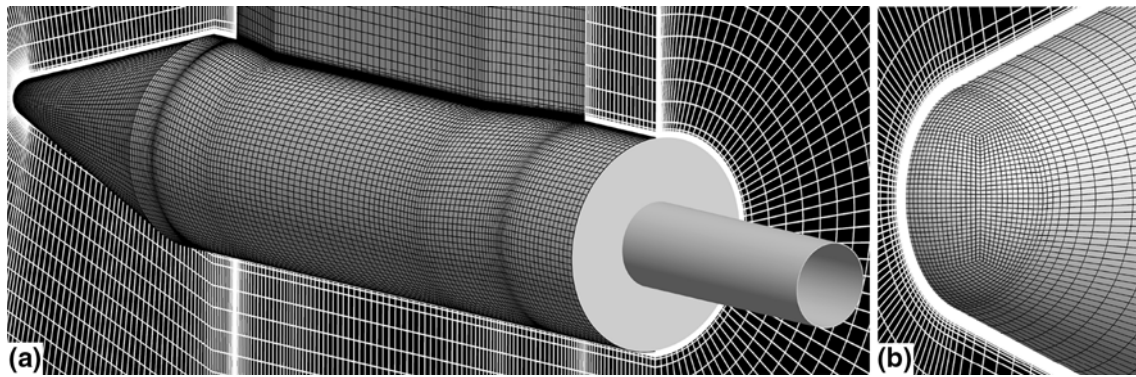**Fig. 2** Flow field decomposition into RANS and LES zones

**Fig. 3** **a** Computational grid for the RANS zone along the main body; **b** avoiding grid singularity at the rotational axis in the nose region. Every 4th grid point is shown
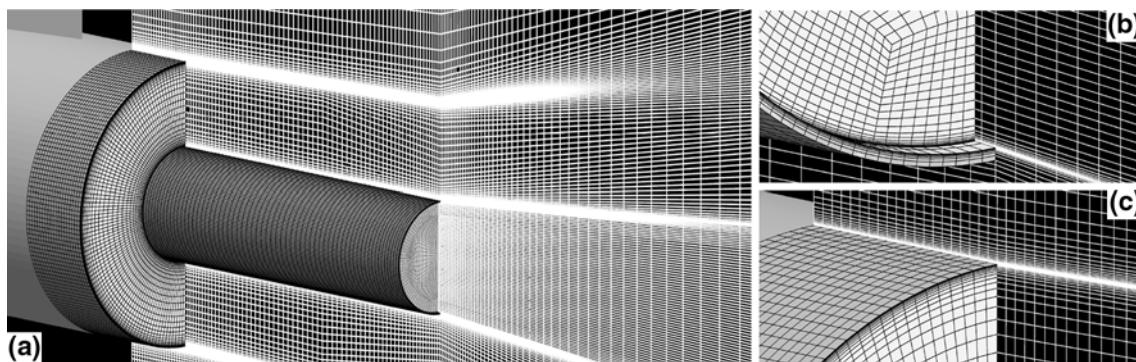


**Fig. 4** **a** Computational grid for the LES zone in the wake of the rocket configuration with jet; **b** nozzle exit region; **c** main body shoulder region. Every 4th grid point is shown

**Table 2** Cell sizes in inner and outer coordinates for RANS and LES zones

|       | $\Delta x/l^+$ | $\Delta r/l^+$ | $\Delta z/l^+$ | $\Delta x/\delta$ | $\Delta y/\delta$ | $\Delta z/\delta$ |
| ----- | -------------- | -------------- | -------------- | ----------------- | ----------------- | ----------------- |
| RANS  | 60             | 0.7            | 60             | 0.1               | $1.7 \times 10^{-3}$ | 0.1            |
| LES   | 30             | 0.7            | 20             | 0.05              | $1.7 \times 10^{-3}$ | 0.03           |

The maximum grid resolution for the RANS and LES zones is given in Table 2 in inner and outer coordinates. In total, the RANS and LES meshes possess 14.8, 23.4, 22.2, and 23.2 Mio. points for the domains of the main body, blunt base, nozzle dummy, and jet flow configurations.

## 4 Results

The presented results are divided into three sections. First, a brief description of the flow along the main body including an estimate of the impact of the vertical strut needed for the wind tunnel tests is given in Sect. 4.1 Additionally, the wake flow topologies of the three investigated configurations are qualitatively described by means of instantaneous and time-averaged velocity distributions.

In Sect. 4.2, numerical results are validated by a comparison to experimental data, where results of the high-speed schlieren measurements provided by DLR Cologne are compared to the time-resolved numerical schlieren pictures. A detailed description of the pressure distribution along the base and outer nozzle contour as well as corresponding spectral analyses including a comparison to the experimental data from DLR Cologne are presented in Sect. 4.3. Finally, three investigated aft-body extensions are compared to each other in Sect. 4.4 with respect to practically relevant wake flow characteristics such as the effects on the pressure drag coefficient as well as mechanical and thermal loads on the rocket structure.

### 4.1 General characterization of the flow field topology

To illustrate the flow topology around the investigated generic rocket models, the instantaneous Mach number and wall pressure coefficient distributions are presented in Fig. 5 (left) for the configuration with a nozzle jet. First, the incoming freestream with $\mathrm{Ma}_\infty = 6.0$ is deflected at the tip parallel to the cone wall forming a detached bow shock, leading to an increase of the pressure. At the
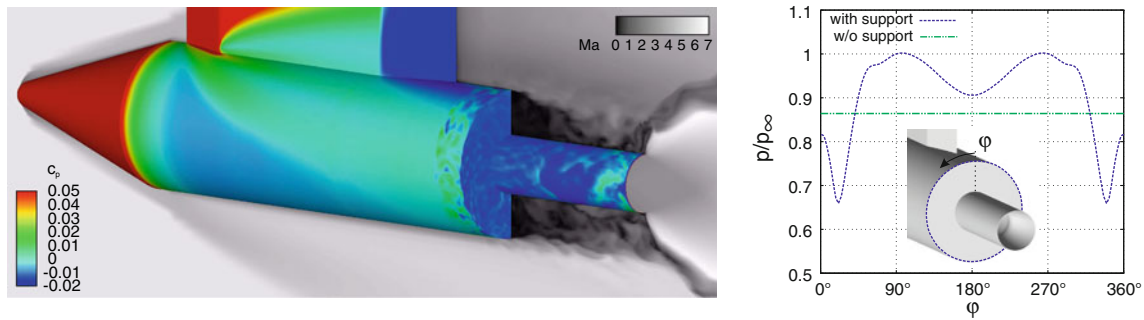
**Fig. 5** Configuration with jet. *Left* instantaneous Ma (*black* and *white*) and $c_p$(*color*) distribution. *Right* circumferential pressure distribution on the base shoulder compared to an axisymmetric case

junction to the cylindrical part, the flow is redirected parallel to the freestream by an expansion fan causing the pressure to decrease again. On the upper side, a second shock and expansion wave system is formed around the double-wedge profiled strut which subsequently interacts with the shock and expansion waves emanating from the main body. As a footprint of this interaction, the non-axisymmetric distribution of the wall pressure can be used to assess the impact of the vertical support on the flow field. The comparison of the azimuthal distribution of the wall pressure along the base shoulder to that of an axisymmetric case shown in Fig. 5 (right), indicates that the influence of the vertical support is non-negligible even on the strut averted side. For this reason, the performed numerical simulations incorporate the vertical support from the experimental investigations.

The wake flow fields of the investigated configurations are determined to a large extent by the expansion of the supersonic shear layers shed from the base shoulder which causes a formation of low pressure regions and subsonic recirculation zones. Besides the observed non-axisymmetric pressure distribution due to the interaction between shock and expansion wave systems of the main body and the strut, the strut wake itself possesses a particularly low specific momentum ($\rho u|_{\phi=0^\circ}/\rho u|_{\phi=180^\circ} = 0.14$ outside of the main body boundary layer). This results in a stronger deflection of the weakened flow towards the axis of axisymmetry on the strut side downstream of the expansion on the base shoulder, which leads to an earlier and more pronounced reattachment compared to the rest of the circumference as described below.

Three wake flow topologies corresponding to the aftbody extensions, i.e., a blunt base, a nozzle dummy, and full-flowing TIC-nozzle, are compared to each other by means of instantaneous and time-averaged velocity distribution presented in Fig. 6. In the blunt base case the expansion and following free reattachment of the shedding shear layer at $x/D = 0.75$ causes a formation of a single recirculation bubble with one toroidal vortex. The effect of a nozzle dummy is to

replace the pure wake structure by a free shear layer interacting with a surface such that a wall-bounded shear layer develops. This is a reattachment on the wall at about $x/D = 0.6$ and a second recirculation region appears at the rear end of the nozzle dummy. More pronounced changes occur when a strongly aft-expanding jet plume emanates from the nozzle leading to a displacement effect on the base flow. As a result, the shedding main body shear layer is reflected away from the nozzle wall and no reattachment occurs, except the mentioned azimuthally tight zone on the strut side determined by a low specific momentum. Thus a confined subsonic cavity region is formed between the base and jet plume in the axial as well between the nozzle wall and shear layer in the radial direction.

The comparison of the instantaneous and time-averaged flow fields shown in Fig. 6 illustrates that the recirculation areas of all three configurations possess a highly dynamic stochastic as well as periodic behavior. The large vortices are clearly developed only in the time-averaged field. A detailed analysis of the significant dynamic characteristics is carried out in following.

### 4.2 Recompression shock oscillation

A comparison of the numerical results to the experimental data from high-speed schlieren measurements of Saile et al. [21] on the blunt base and nozzle dummy configurations is performed by means of numerical schlieren pictures. In analogy to the experiment, the numerically computed density gradient is used to detect the recompression shock positions which show a good agreement with the experimental results, Figs. 7 and 8.

Due to the interaction with the recirculation zone and shed shear layers, the recompression shock strongly oscillates in time. A spectral analysis of this oscillation in the radial direction is performed for four axial positions on the strut averted side for the blunt base and the nozzle dummy configuration, Figs. 9 and 10. Both configurations feature a distinct peak around $Sr_D = 0.2$ that corresponds to a
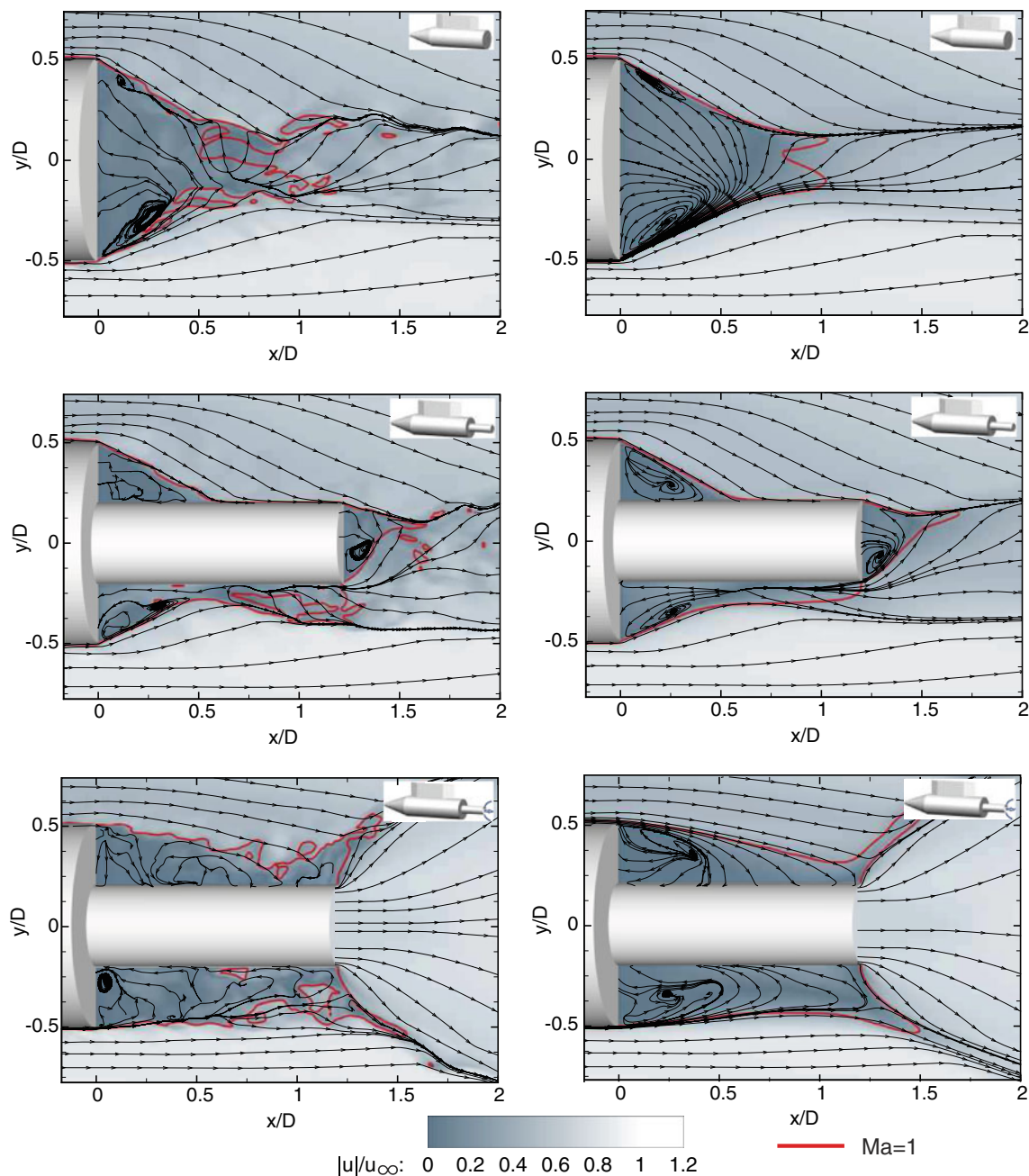
**Fig. 6** Instantaneous (*left*) and time-averaged (*right*) axial velocity distributions in the symmetry plane of the blunt base (*top*), nozzle dummy (*center*) and jet (*bottom*) configurations

typical von Kármán vortex shedding mode which is also detected by the experiments at DLR Cologne. The low frequency peaks of weaker intensity at about $Sr_D = 0.1$ are clearly pronounced for the nozzle dummy configuration and are presumably caused by the vertical flapping motion of the shear layer as known from the literature and former investigations performed on a similar configuration but an endless nozzle extension [22, 23]. The same mode at lower

intensity is also found for the blunt base configuration at higher distances from the base ($x/D = 1.5$ and 2.0), while near the base region ($x/D = 1.0$ and 1.25) the low frequency modes shift to $Sr_D = 0.05$. Other less distinct peaks at higher frequencies present for both configurations, e.g., $Sr_D = 0.4$, $Sr_D = 0.7$, $Sr_D = 0.9$, are assumed to be caused by a superposition of several dynamic processes within the wake.
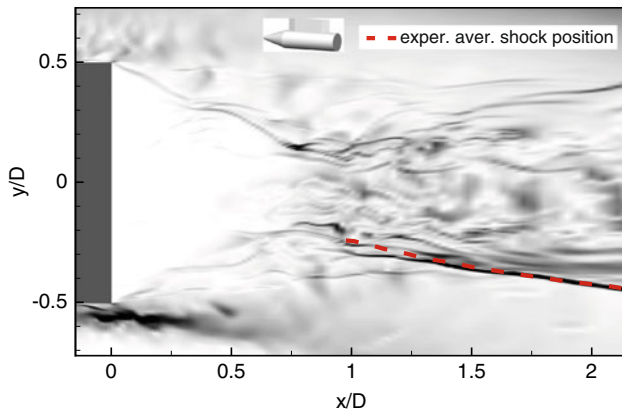
Fig. 7 Numerical schlieren picture in the symmetry plane of the blunt base configuration. Experimental result is indicated by the *dashed line*
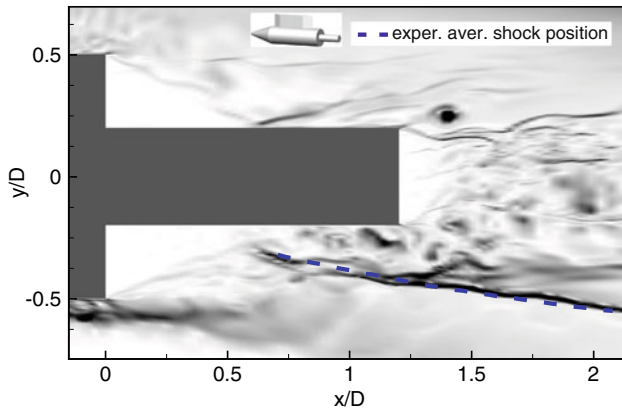


Fig. 8 Numerical schlieren picture in the symmetry plane of the nozzle dummy configuration. Experimental result is indicated by the *dashed line*
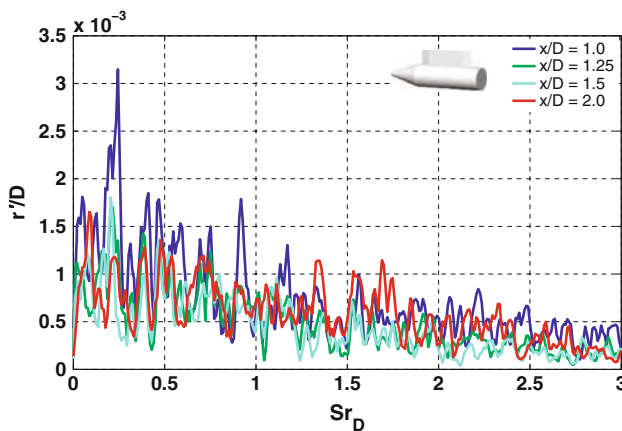


Fig. 9 Spectra of the recompression shock oscillation of the blunt base configuration
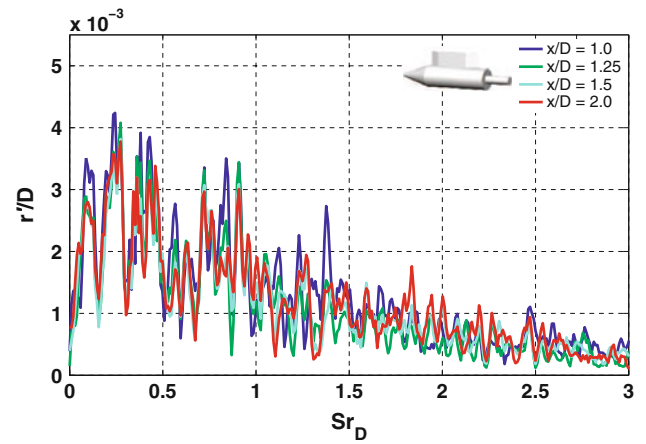


Fig. 10 Spectra of the recompression shock oscillation of the nozzle dummy configuration

### 4.3 Spatial and temporal analysis of wall pressure distribution

The low pressure region at the base associated with the recirculation zone due to the flow separation is responsible for the base drag and the time-averaged loads on the outer nozzle wall. The turbulent highly dynamic character of the wake leads to significant wall pressure oscillations and, consequently, dynamic loads which may excite critical structural modes. Therefore, an accurate prediction of the static and dynamic wall pressure level and understanding of its dependence on different aft-body extensions is of particular interest.

An overview of the mean wall pressure and root mean square (rms) values of the wall pressure fluctuations is presented in Figs. 11 and 12 for the blunt base, Figs. 13 and 14 for the nozzle dummy and Figs. 15 and 16 for the jet configuration. Due to the estimated strong influence of the strut on the wake flow along the whole circumference, the values are considered in the radial and axial directions at five azimuthal positions which are chosen accordingly to
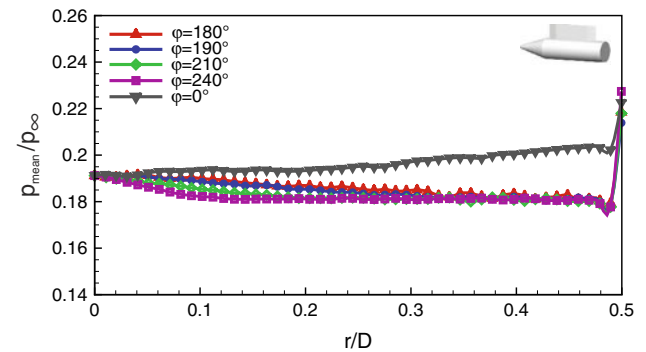


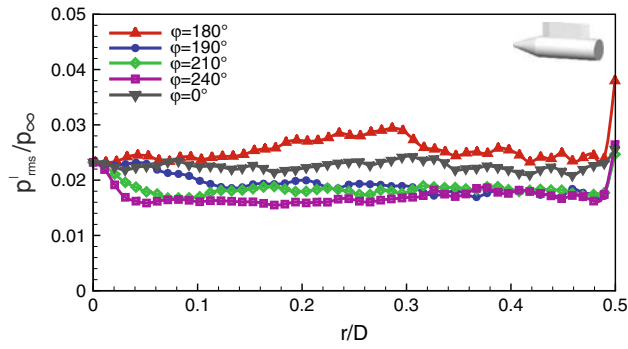Fig. 11 Time-averaged wall pressure distribution for the blunt base configuration

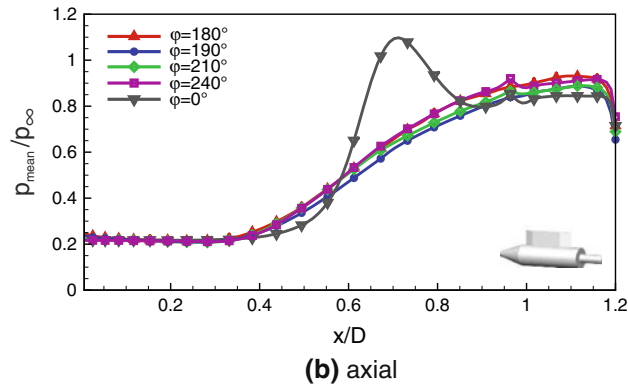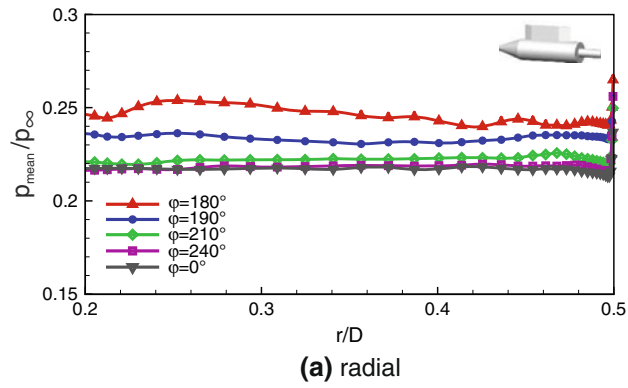**Fig. 12** rms value of the wall pressure fluctuations for the blunt base configuration



**(a)** radial



**(a)** radial



**(b)** axial



**(b)** axial

**Fig. 13** Time-averaged wall pressure distribution for the nozzle dummy configuration

**Fig. 14** rms value of the wall pressure fluctuations for the nozzle dummy configuration



**(a)** radial



**(b)** axial

**Fig. 15** Time-averaged wall pressure distribution for the jet configuration

the experimental setup of DLR Cologne with $\phi = 0°$ being the azimuthal position of the strut.

Considering the pressure distribution along the base wall, the blunt base configuration features a nearly constant and azimuthally almost homogeneous radial distribution of the mean and rms values of the base pressure of about $p/p_\infty = 0.2$ and $p'_{rms}/p_\infty = 0.02$. Adding a nozzle dummy causes a slight increase of the mean base pressure level up to $p/p_\infty = 0.25$ as well as a stronger dependence of the mean and rms values of the base pressure on the circumferential position. The latter effect is also present at the jet
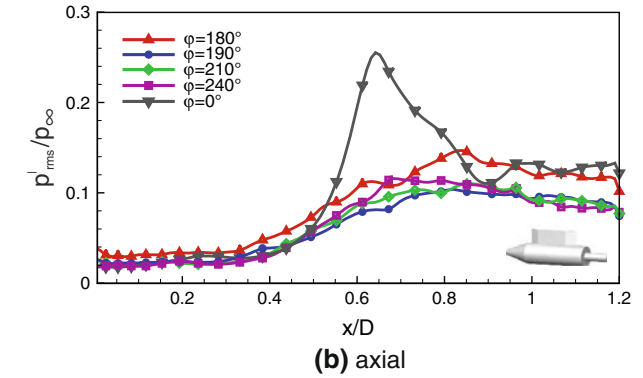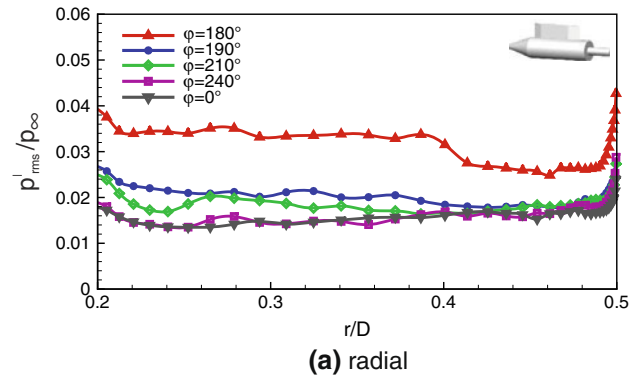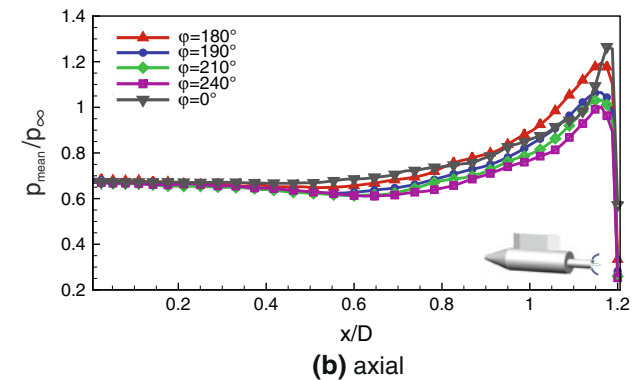
**(a)** radial



**(b)** axial

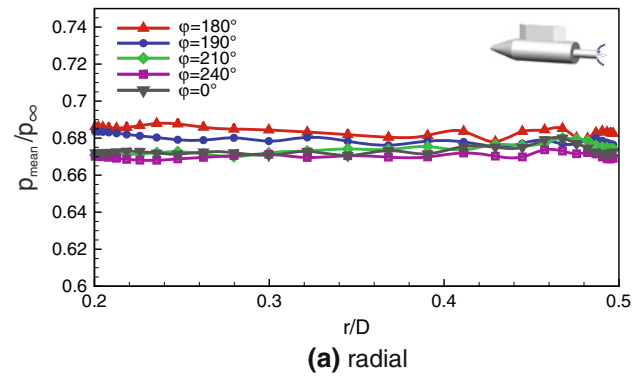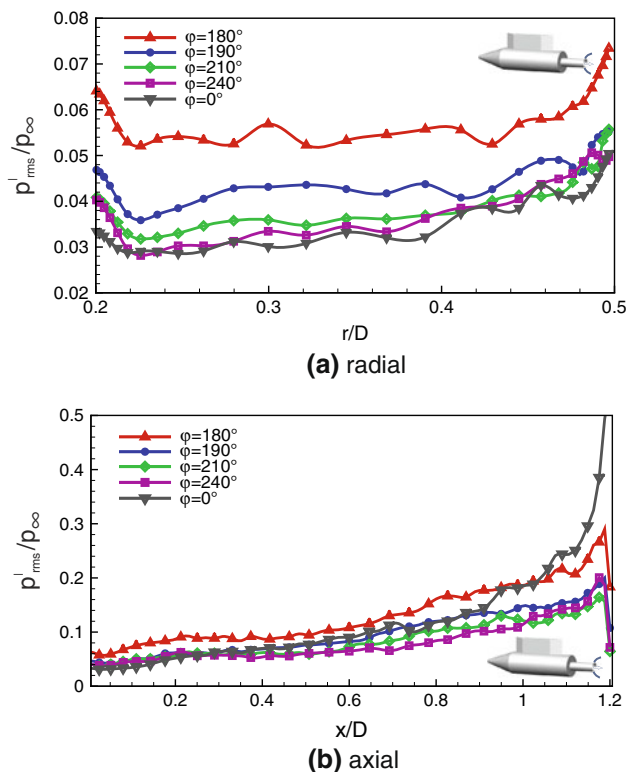Fig. 16 rms value of the wall pressure fluctuations for the jet configuration
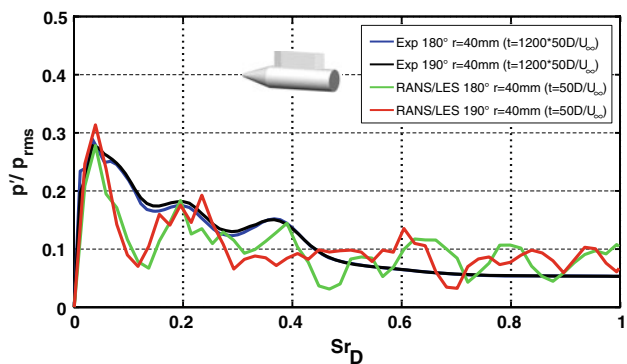


Fig. 17 Comparison of the numerical and experimental base pressure spectra for the blunt base configuration

configuration and is obviously caused by the suppression of a pressure balance in the radial direction due to a geometric obstacle such as the outer nozzle wall. In addition, it is worth mentioning that the computed higher levels of the pressure fluctuations on the strut averted side are also observed in the experiments [21] and are presumably caused by non-axisymmetric effects of the vertical strut on the velocity field around the main body. However, the increase of the pressure fluctuations along the circumference from 190° to 180° in the experiments is slightly lower than in the simulations, which can be explained by using only a half model with symmetry conditions in the
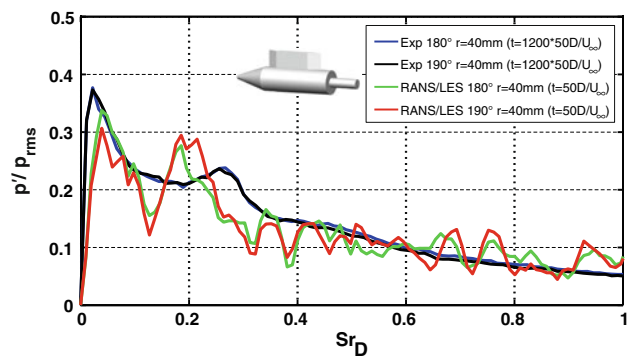


Fig. 18 Comparison of the numerical and experimental base pressure spectra for the nozzle dummy configuration

computation where a full model is investigated in the experiment.

Considering the pressure distribution along the outer nozzle wall, the nozzle dummy configuration indicates a clearly pronounced increase of the mean and rms values of the wall pressure in the streamwise direction. This is caused by a solid reattachment of the shear layer at about $x/D = 0.6$ with higher levels at 0° due to a stronger deflection and, consequently, a more pronounced impingement of the strut wake on the nozzle surface as discussed in Sect. 4.1 The configuration with jet features apart from the azimuthally tight region on the strut side a recirculation cavity with no solid reattachment and huge vortex in the time-averaged field filling almost the whole cavity area. As illustrated in Fig. 6 in Sect. 4.1, the back-flow velocity induced by that vortex has its maximum at about $x/D = 0.6$–0.8 leading to a slight decrease of the wall pressure compared to the region near the base. Further upstream, the displacement effect of the strongly aft-expanding jet plume results in the rise of the wall pressure up to its maximum of about $p/p_\infty = 1.2$ near the nozzle exit. The mixing zone of the shear layer emanating from the nozzle with the shear layer shedding from the rocket base is determined by high velocity gradients. These cause the production of turbulent structures which travel upstream within the subsonic recirculation region and excite the pressure fluctuations. Correspondingly, the rms values of the wall pressure feature maxima near the nozzle exit and constantly decrease in the upstream direction as a result of the decay of the turbulent structures due to viscous effects.

To gain insight into the dominant modes of the observed dynamic behavior, a DFT (Discrete Fourier Transformation) of the numerically computed wall pressure fluctuations is performed and compared to the spectra of the experimental wall pressure oscillations provided by DLR Cologne for the blunt base and nozzle dummy configuration.

To compare numerical and experimental pressure signals, the latter are divided into equal segments at a length of the corresponding numerical signal and subjected to its own DFTs. The arithmetic mean is compared to the numerical spectra.

The comparison of the numerical and experimental wall pressure spectra of the blunt base configuration is shown in Fig. 17 and indicates a good match between the performed simulation and experiment. Three distinct peaks at $Sr_D = 0.05$, $Sr_D = 0.2$, and $Sr_D = 0.35$ are identified in the blunt base case. The nozzle dummy configuration features two dominant modes at $Sr_D \approx 0.04$ and $Sr_D = 0.2$ and also indicates a satisfactory agreement with the experimental data, Fig. 18. The obtained peaks around $Sr_D = 0.2$ are well-known as a vortex shedding frequency. The additional low-frequency peaks around $Sr_D = 0.04$–$0.05$ are believed to be caused by the inner motion of the large scale vortex within the separation bubble [22].

## 4.4 Comparative analysis of aft-body extensions

After the detailed analysis of the wake flow field characteristics, a comparison of three investigated configurations to each other is of practical interest. As shown in the previous section, the base regions of the investigated configurations are determined to a great extent by separating and reattaching shear layers. The strength of the resulting recompression shocks and expansion waves directly depends on the deflection of the flow which is determined by the tail geometry and other geometric obstacles, e.g., a strongly aft-expanding jet plume.

The expansion of the shed shear layer on the rocket shoulder has a direct effect on the base pressure level that constitutes a major part of the base drag. From Fig. 6 in Sect. 4.1 it is clear that the blunt base configuration features the maximum radial deflection of the shed shear layer towards the rocket axis on the strut averted side which results in the minimum value of the base pressure levels among the investigated configurations of about $p/p_\infty \approx 0.2$ as illustrated in Fig. 19. Adding the nozzle dummy only slightly reduces the radial deflection of the flow on the strut averted side compared to the blunt base case, which results in a slightly higher level of the base pressure of $p/p_\infty \approx 0.25$. A significant increase of the base pressure level to $p/p_\infty \approx 0.7$ occurs for the jet configuration as a result of the displacement effect of the strongly aft-expanding jet plume that causes only a minimum radial deflection of the shear layer towards the rocket axis and leads to a formation of the cavity. When extrapolated to an axisymmetric case, the detected base pressure ratios lead to the base pressure drag coefficients of $C_{Dp\ base} = 0.032$ (blunt base), $0.030$ (nozzle dummy), and $0.012$ (jet configuration) illustrating the effect of the attached aft-body configurations on the base drag.
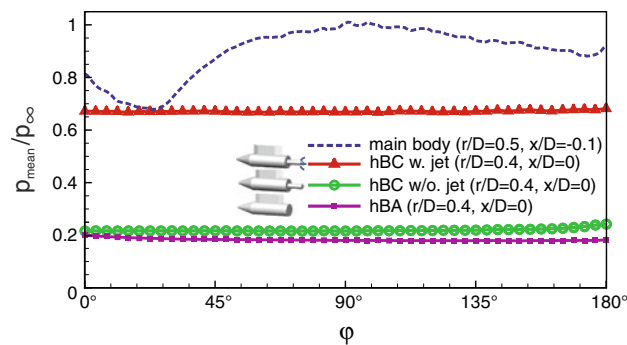


**Fig. 19** Comparison of the mean base pressure level for three different aft-body extensions including the mean pressure level on the main body wall
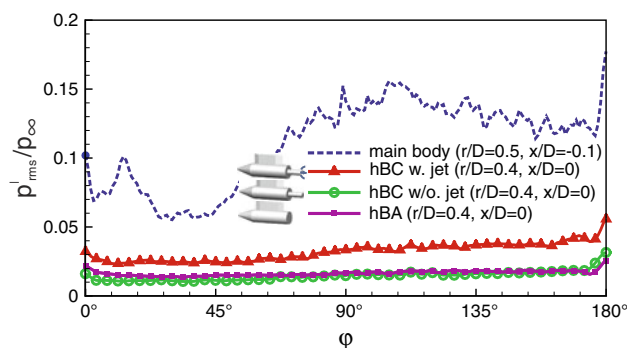


**Fig. 20** Comparison of the rms values of the base pressure for three different aft-body extensions incl. the rms values on the main body wall

The pressure drag coefficient of the investigated fore body extrapolated to an axisymmetric case is considerably higher due to the formation of a strong bow shock at $Ma_\infty = 6$ and measures $C_{Dp\ body} = 0.22$. Thus, the base flow constitutes between 5.2 and 12.7% of the overall pressure drag depending on the attached aft-body extensions.

Regarding the effects of the aft-body extensions on the dynamic character of the base pressure, a similar behavior as for the mean values is observed. The rms values of the base pressure fluctuation slightly increase from $p'_{rms}/p_\infty \approx 0.02$ for the blunt base to $p'_{rms}/p_\infty \approx 0.025$ for the nozzle dummy configuration and reach a maximum of $p'/p_\infty \approx 0.05$ for the configuration with jet, Fig. 20. Note that compared with the pressure fluctuations on the main body at $x/D = 0.1$ (blue dashed line), the absolute amplitudes of the pressure oscillation on the base wall are considerably lower than in the incoming turbulent supersonic boundary layer with its $p'_{rms}/p_\infty \approx 0.1$. Unlike the incoming turbulent boundary layer, the base pressure fluctuations, however, feature a pronounced periodic behavior as discussed before and therefore, should be taken into account during the rocket design regarding the eigenfrequency of the mechanical structure of the space launcher.

The wall pressure oscillations are significantly higher on the nozzle wall as indicated in Figs. 21 and 22. The reattachment causes the corresponding rms values for the nozzle dummy configuration to reach up to $p'_{rms}/p_\infty \approx 0.15$ slightly upstream of the reattachment point and remain at a level of about 10 % of the freestream mean value up to the end of the nozzle extension. The configuration with an aft-expanding jet features an even higher pressure fluctuation level of up to $p'_{rms}/p_\infty \approx 0.3$ near the nozzle exit. This is caused by turbulent structures generated in the mixing zone of the main body and jet flow shear layers that impinge upon the wall. The detected high levels of pressure fluctuations lead to dynamic radial loads on the nozzle wall. In an axisymmetric case they also may cause side loads on the whole nozzle extension as the pressure fluctuations are normally shifted in phase in the circumferential direction. Due to the low value of the ambient pressure at Ma = 6, these phenomena are, however, not as critical as in the transonic flight regime where the structural loads peak.

Although the hypersonic part of the flight trajectory is less critical from the structural point of view, the mixing of the ambient flow with the jet plume's shear layer and subsequent impingement of the turbulent structures
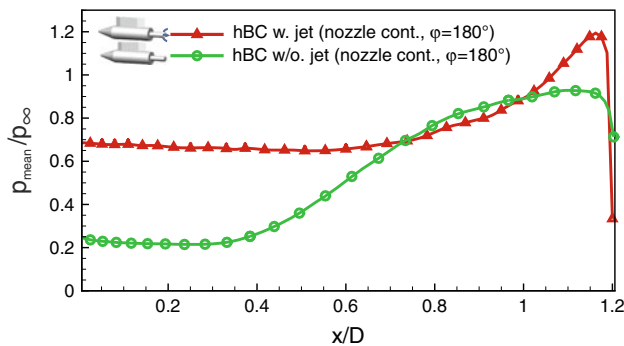
generated in the mixing zone on the nozzle may cause strong thermal loads. As demonstrated by the axial velocity distribution in Fig. 6 in Sect. 4.1, the hot plume gases will feed in a real case the cavity-formed recirculation area with additional thermal energy which will be convected up to the base area. This aspect is not analyzed quantitatively in the present paper since the corresponding experiments incorporate a jet flow at a temperature of $\sim 200$ K at the nozzle exit. It will be analyzed in a new research project starting 2013. In this future investigation, the jet configuration possesses a hot helium nozzle flow at 800 K leading to more realistic conditions due to low molar mass and higher temperature. Experiments and simulations will be performed by the authors in cooperation with the University of Braunschweig to analyze the thermodynamic phenomena in the wake of space launchers at supersonic freestream conditions.

## 5 Conclusions

The turbulent wake flows of three supersonic generic space launcher configurations differing in the attached aft-body extensions were compared to analyze the influence of the nozzle and aft-expanding jet on the base flow physics. Within the zonal RANS/LES method, a time-averaged RANS method was used for the computation of the attached main body flow, while a time-resolved LES was performed for the highly unsteady and separated wake zones.

The flow field around the main body of the investigated generic configurations is dominated by the interaction of two systems of shocks and expansion waves, which are generated by the axisymmetric rocket body and the vertical strut support, and differs from an axisymmetric case even in the strut averted region.

Depending on the applied aft-body extensions, the time-averaged base pressure level, which constitutes a major part of the base drag, ranges from $p/p_\infty \approx 0.2 - 0.25$ for the blunt base and nozzle dummy configurations up to $p/p_\infty \approx 0.7$ for the configuration with a strongly aft-expanding jet leading to a decrease of the base pressure drag coefficient from $C_{Dp\ base} = 0.032$ to 0.012, when extrapolated on an axisymmetric case, corresponding to 12.7 and 5.2 % of the overall pressure drag of the launcher respectively. The rms values of the base pressure span from $p'/p_\infty \approx 0.02$ for the configurations without jet up to $p'/p_\infty \approx 0.05$ for the configuration with jet. Compared with the pressure fluctuations in the turbulent hypersonic shear layer, the pressure oscillations on the base wall are considerably lower. However, the wall pressure oscillations are significantly higher when considering the nozzle wall. Due to reattachment the corresponding rms values for the



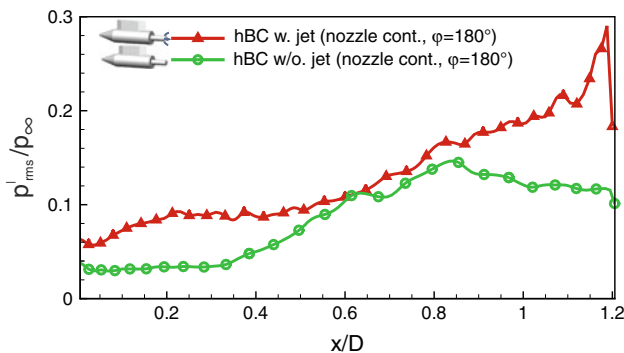**Fig. 21** Comparison of the mean pressure along the outer nozzle wall for the nozzle dummy and jet configuration



**Fig. 22** Comparison of the rms values of the pressure oscillations along the outer nozzle wall for the nozzle dummy and jet configuration

nozzle dummy configuration reach up to $p'_{rms}/p_\infty \approx 0.15$. The configuration with an aft-expanding jet features an even higher pressure fluctuation level of up to $p'_{rms}/p_\infty \approx 0.3$ which is caused by turbulent structures generated in the mixing zone of the main body and jet flow shear layers that impinge upon the wall. Due to the low ambient pressure at $Ma_\infty = 6$, the resulting mechanical loads are less critical than the caused convection of jet plume's gases into the base region, which might define an important thermal issue in case of a real launcher.

The presented spectral analysis of wake flow characteristics such as oscillations of the recompression shock positions and base pressure signals showed a good agreement with the experimental data provided by DLR Cologne. Several distinct modes, e.g., $Sr_D = 0.1$ (shear layer flapping) and $Sr_D = 0.2$ (von Kármán vortex shedding), were identified indicating a pronounced periodic behavior of the base flow dynamics. The most dominant peaks of the base pressure fluctuations were observed at very low Strouhal numbers of about $Sr_D \approx 0.05$ and referred to the motion of large scale vortices within the recirculation bubble.

# References

1. Rollstin, L.: Measurement of inflight base-pressure on an artillery-fired projectile. AIAA Paper, pp. 287–2427 (1987)
2. Mathur, T., Dutton, J.C.: Base-bleed experiments with a cylindrical afterbody in supersonic flow. J. Spacecr. Rockets **33**, 30–37 (1996)
3. Bannink, W.J., Houtman, E.M., Bakker, P.G.: Base flow/under-expanded exhaust plume interaction in a supersonic external flow. AIAA Paper, pp. 98–1598 (1998)
4. Scarano, F., van Oudheusden, B.W., Bannink, W.J., Bsibsi, M.: Experimental investigation of supersonic base flow plume interaction by means of particle image velocimetry. In: 5th European Symposium on Aerothermodynamics for Space Vehicles, Germany (2004)
5. Benay, R., Servel, P.: Two-equation k–σ turbulence model: application to a supersonic base flow. AIAA J. **39**, 407–416 (2001)
6. Papp, J.L., Ghia, K.N.: Application of the RNG turbulence model to the simulation of axisymmetric supersonic separated base flows. AIAA Paper, pp. 2001–2027 (2001)
7. Forsythe, J.R., Hoffmann, K.A., Cummings, R.M., Squires, K.D.: Detached-eddy simulation with compressibility corrections applied to a supersonic axisymmetric base flow. J. Fluid Eng. **124**, 911–923 (2002)
8. Kawai, S., Fujii, K.: Computational study of a supersonic base flow using LES/RANS hybrid methodology. AIAA Paper, pp. 2004–2068 (2004)
9. Fureby, C., and Kupiainen, K.: Large-Eddy simulation of supersonic axisymmetric baseflow. In: Turbulence Shear Flow Phenomenon Japan (2003)
10. Sandberg, R.D., Fasel, H.F.: High-accuracy DNS of supersonic base flows and control of the near wake. In: Users Group Conference, IEEE Computer Society, pp. 96–104 (2004)
11. Sandberg, R.D., Fasel, H.F.: Numerical investigation of transitional supersonic axisymmetric wakes. J. Fluid Mech. **563**, 1–41 (2006)
12. Sandberg, R.D.: Numerical investigation of turbulent supersonic axisymmetric wakes. J. Fluid Mech. **702**, 488–520 (2012)
13. Boris, J.P., Grinstein, F.F., Oran, E.S., Kolbe, R.L.: New insights into large eddy simulation. Fluid Dyn. Res. **10**, 199–228 (1992)
14. Liou, M.S., Steffen, C.J. Jr.: New flux splitting scheme. J. Comp. Phys. **107**, 23–39 (1993)
15. Meinke, M., Schröder, W., Krause, E., Rister, Th.: Comparision of second- and sixth-order methods for large-eddy simulations. Comput. Fluids **31**, 695–718 (2002)
16. Fares, E., Schröder, W.: A general one-equation turbulence model for free shear and wall-bounded flows. Flow Turbul. Combust. **73**, 187–215 (2004)
17. Roidl, B., Meinke, M., Schröder, W.: Reformulated synthetic turbulence generation method for a zonal RANS-LES method and its application to zero-pressure gradient boundary layers. Int. J. Heat Fluid Flow. doi:10.1016/j.ijheatfluidflow.2013.03.017 (2013)
18. Roidl, B., Meinke, M., Schröder, W.: Reformulated synthetic turbulence generation method for a zonal RANS-LES method and its application to non-zero-pressure gradient boundary layers. Int. J. Heat Fluid Flow (2013, in press)
19. Jarrin, N., Benhamadouche, S., Laurence, D., Prosser, R.: A synthetic-eddy-method for generating inflow conditions for large-eddy simulations. J. Heat Fluid Flow **27**, 585–593 (2006)
20. Pamiès, M., Weiss, P.-É., Garnier, E., Deck, S., Sagaut, P.: Generation of synthetic turbulent inflow data for large eddy simulation of spatially evolving wall-bounded flows. Phys. Fluids **16**, 045103 (2009)
21. Saile, D., Gülhan, A., Henckels, A.: Investigations on the near-wake region of a generic space launcher geometry. AIAA Paper, pp. 2011–2352 (2011)
22. Saile, D., Gülhan, A., Henckels, A., Glatzer, C., Statnikov, V., Meinke, M.: Investigations on the turbulent wake of a generic space launcher geometry in the hypersonic flow regime. In: Progress in flight physics. Advances in aerospace sciences EUCASS book ser. 5, pp. 209–234 (2013). doi:10.1051/eucass/201305209
23. Statnikov, V., Glatzer, C., Meiß, J.-H., Meinke, M., Schröder, W.: Numerical investigation of the near wake of generic space launcher systems at transonic and supersonic flows. In: Progress in Flight Physics. Advances in aerospace sciences EUCASS book ser 5, pp. 191–208 (2013). doi:10.1051/eucass/201305191